

Low-Temperature Heat Transport under Phonon Confinement in Nanostructures

M. Sidorova,^{1,2,3,*} A.D. Semenov,³ A. Zaccane,^{4,5} I. Charaev,⁶
M. Gonzalez,⁶ A. Schilling,⁶ S. Gyger,^{7,8} and S. Steinhauer⁷

¹Nanyang Technological University, School of Physical and Mathematical Science, 21 Nanyang Link, 637371 Singapore

²Humboldt-Universität zu Berlin, Department of Physics, Newtonstr. 15, 12489 Berlin, Germany

³German Aerospace Center (DLR), Institute of Optical Sensor Systems, Rutherfordstr. 2, 12489 Berlin, Germany

⁴Department of Physics "A. Pontremoli", University of Milan, via Celoria 16, 20133 Milan, Italy

⁵Institute for Theoretical Physics, University of Göttingen, Friedrich Hund Platz 1, 37077 Göttingen, Germany

⁶Physics Institute, University of Zürich, Winterthurerstrasse 190, 8057 Zürich, Switzerland

⁷Department of Applied Physics, KTH Royal Institute of Technology, SE-106 91 Stockholm, Sweden

⁸Ginzton Laboratory, Stanford University, 348 Via Pueblo Mall, Stanford, California 94305, USA

(Dated: October 14, 2024)

Heat transport in bulk materials is well described using the Debye theory of 3D vibrational modes (phonons) and the acoustic match model. However, in cryogenic nanodevices, phonon wavelengths exceed device dimensions, leading to confinement effects that standard models fail to address. With the growing application of low-temperature devices in communication, sensing, and quantum technologies, there is an urgent need for models that accurately describe heat transport under confinement. We introduce a computational approach to obtain phonon heat capacity and heat transport rates between solids in various confined geometries, that can be easily integrated into, e.g., the standard two-temperature model. Confinement significantly reduces heat capacity and may slow down heat transport. We have validated our model in experiments on strongly disordered NbTiN superconducting nanostructures, widely used in highly efficient single-photon detectors, and we argue that confinement is due to their polycrystalline granular structure. These findings point to potential advances in cryogenic device performance through tailored material and microstructure engineering.

I. INTRODUCTION

Low-temperature devices, including superconducting and hybrid quantum sensors for particles [1] and photons [2], circuits [3], and electronics [4] have become integral to quantum technology, detection, sensing, and metrology. For instance, superconducting nanostrip single-photo detectors (SNSPDs, commonly known as nanowire detectors) cascaded into kilo-pixel arrays enable quantum imaging [5], while advanced superconducting digital electronics [6] with sophisticated layering and miniaturization are expected to outperform CMOS technology in high-performance computing. However, as device complexity grows, so does excess heat dissipation coupled with cryogenic limitations in heat removal, driving these devices beyond their optimal operation. While heat transport in crystalline bulk materials is well understood through the Debye theory of 3D vibrational modes (phonons) [7], in cryogenic nanodevices, phonon wavelengths approach device dimensions causing confinement, which standard heat transport models fail to address.

Confinement imposed by device geometry restricts vibrational modes, altering the thermal properties of solids and affecting heat transport at a large scale. Experimental works have demonstrated various confinement effects, such as changes in the frequency scaling of vibrational density of states in a few nanometer-thick films of amorphous ice at 120 K [8]; reduced thermal conductivity in

sub-20 nm (Ge-Si core-shell) nanowires between 100 and 300 K [9]; enhanced specific heat in 2 nm lead grains below 10 K [10]. Advanced thermal imaging techniques, like SQUID-on-tip thermometry, have spatially resolved heat dissipation at individual defects in 2D graphene [11, 12].

Sparse theoretical efforts addressed the problem. Early studies [13, 14] derived phonon heat capacity by counting vibrational modes in spherical grains, showing that surface quality (suspended versus clamped) significantly impacts heat capacity through the presence or absence of surface modes. Later works [15, 16] expanded this to nanostructures of varying sizes and shapes. The vibrational density of states in thin films was derived in Ref. [8] based on the confinement model from Ref. [17]. The same model [17] also explains diverse phenomena such as shear elasticity in confined liquids [18], suppression of THz modes and reduced dielectric permittivity in nanoconfined media such as water and ferroelectric films [19, 20], as well as reduced heat capacity in thin films [21] (see a comment [22]). More recent works described heat removal for metallic grains embedded in dielectric matrices [23] and heat dissipation in moderately disordered mesoscopic systems [24–26], showing enhanced electron-phonon cooling due to scattering at individual defects and a shift in Joule heating and electron cooling profiles relative to the defect center. Despite these efforts, a comprehensive model for heat transport under confinement across diverse geometries and materials is still lacking.

In this work, we derive explicit expressions for phonon heat capacity and heat transport rates between solids for various confined geometries. We validate our ap-

* Mariia.Sidorova@dlr.de

proach using experimental data from strongly disordered NbTiN superconducting nanostructures, widely used in highly efficient single-photon detectors [2]. We also provide physical insights on how confinement affects cryogenic nanodevice performance, suggesting strategies for optimization.

II. MODEL OF HEAT TRANSPORT UNDER PHONON CONFINEMENT

Below we address confinement in thin films and cylinders, dragging an idea from [17]. We derive expressions for the phonon heat capacity and the escape time of phonons from the sample to the underlying substrate.

A. Phonon heat capacity

For a bulk 3D crystal, the vibrational (phonon) heat capacity per unit volume and per one polarization is given by

$$\begin{aligned} c_{ph}^{(3D)}(T) &= \frac{\partial U}{\partial T} = \int_0^{\omega_D} \frac{\partial}{\partial T} \left(\frac{g(\omega)\hbar\omega}{e^{\hbar\omega/k_B T} - 1} \right) d\omega \\ &= \frac{1}{2\pi^2} k_B \left(\frac{k_B T}{\hbar u} \right)^3 \int_0^{x_D} \frac{x^4 e^x}{(e^x - 1)^2} dx, \quad (1) \end{aligned}$$

where $g(\omega) = \omega^2/(2\pi^2 u^3)$ is the Debye density of states (DOS, per unit volume), k_B and \hbar are the Boltzmann and reduced Planck constants, $\omega_D = (6\pi^2 u^3/a_0^3)^{1/3}$ is the Debye angular frequency, u and a_0 denote the sound velocity and the lattice constant, $x = \hbar\omega/k_B T$. Given the linear dispersion $\omega = uk$ (k is the wavevector), valid at temperatures much lower than the Debye temperature, and a low-temperature approximation $x_D \rightarrow \infty$, the integral in Eq. (1) simplifies to $4\pi^4/15$. This leads to the well-known Debye result: $c_{ph}^{(3D)} = (2\pi^2/15)k_B(k_B T/\hbar u)^3$.

1. c_{ph} , confinement in thin film

For thin films with geometry depicted in Fig. 1a, confinement is imposed by film plains. It restricts phonon states with wavelengths larger than $d/\cos\Theta$, where d is the film thickness, and Θ is the angle measured from the confinement z -axis.

In spherical coordinates of the wavevector k -space, illustrated in Fig. 1c, the wavevectors of restricted phonon states $k_{min} = 2\pi \cos\Theta/d$ define the surface of blue spheres within the Debye sphere. Consequently, this modifies heat capacity that can be described by introducing an angle-dependent integral limit and integrating over the polar angle Θ :

$$\begin{aligned} c_{ph}^{(2D)}(T, d) &= \frac{1}{2\pi^2} k_B \left(\frac{k_B T}{\hbar u} \right)^3 \\ &\times \int_0^{\pi/2} \sin\Theta \int_{x^*(\Theta)}^{x_D} \frac{x^4 e^x}{(e^x - 1)^2} dx d\Theta, \quad (2) \end{aligned}$$

where, $x^*(\Theta) = 2\pi \cos\Theta \hbar u/(d k_B T)$.

Alternatively, one can account for the confinement by modifying the phonon DOS inside a sphere with radius $2\pi/d$ that has been done in previous studies[8, 17, 28], which results in a different expression for the heat capacity Eq. (A1) in Appendix. In the limit of strong confinement ($x^*(0) \rightarrow x_D$ in Eq. (A1)), this alternative approach clearly shows that heat capacity reduces upon decreasing the film thickness and temperature as $c_{ph}^{(2D)} \propto dT^4$. In the bulk limit, where $x(\Theta)^* \rightarrow 0$ in Eq. (2), one retrieves the Debye result. These two limiting cases are seen in Fig. 2a.

2. c_{ph} , confinement in cylinder

A cylindrical confined geometry with a height d and diameter D is illustrated in Fig. 1b. This geometry could be relevant to nanowires (cylinders with infinite height, a confined 1D structure) as well as to films with granular morphology (densely packed confined 0D grains). Cylinder bases restrict phonon states with wavelengths larger than $d/\cos\Theta$ for angles $\Theta \leq \tan^{-1}(D/d)$; we note that for $D = d$, $\Theta = 45^\circ$. In addition, cylinder walls restrict phonon states with wavelengths larger than $D/\sin\Theta$ for larger angles $\Theta \geq \tan^{-1}(D/d)$.

In the k -space, the wavevectors of phonon states restricted by cylinder bases ($k_{min} = 2\pi \cos\Theta/d$) and walls ($k_{min} = 2\pi \sin\Theta/D$) with corresponding conditions on angles, define the surface of blue spheres and red toroid, respectively (see Fig. 1c). These restrictions modify the phonon heat capacity as follows:

$$\begin{aligned} c_{ph}^{(0D)}(T, d, D) &= \frac{1}{2\pi^2} k_B \left(\frac{k_B T}{\hbar u} \right)^3 \\ &\times \left[\int_0^{\tan^{-1}(D/d)} \sin\Theta \int_{x^*(\Theta)}^{x_D} \frac{x^4 e^x}{(e^x - 1)^2} dx d\Theta \right. \\ &\left. + \int_{\tan^{-1}(D/d)}^{\pi/2} \sin\Theta \int_{x^{**}(\Theta)}^{x_D} \frac{x^4 e^x}{(e^x - 1)^2} dx d\Theta \right]. \quad (3) \end{aligned}$$

Here, the lower limit $x^*(\Theta)$ is caused by the confinement along the z direction, and $x^{**}(\Theta) = 2\pi \sin\Theta \hbar u/(D k_B T)$ in the xy -plane.

As the cylinder diameter becomes much larger than its height, $D \gg d$, the integral limits in Eq. (3) $\tan^{-1}(D/d) \rightarrow \pi/2$, and the second term diminishes, retrieving the result for confinement in films. In the opposite limit of strong confinement by the cylinder walls, $D \gg d$, $\tan^{-1}(D/d) \rightarrow 0$, and the first term diminishes, while the second integral in the second term reduces fast as $x^{**}(\Theta) \rightarrow x_D$. These cases are shown in Fig. 2b.

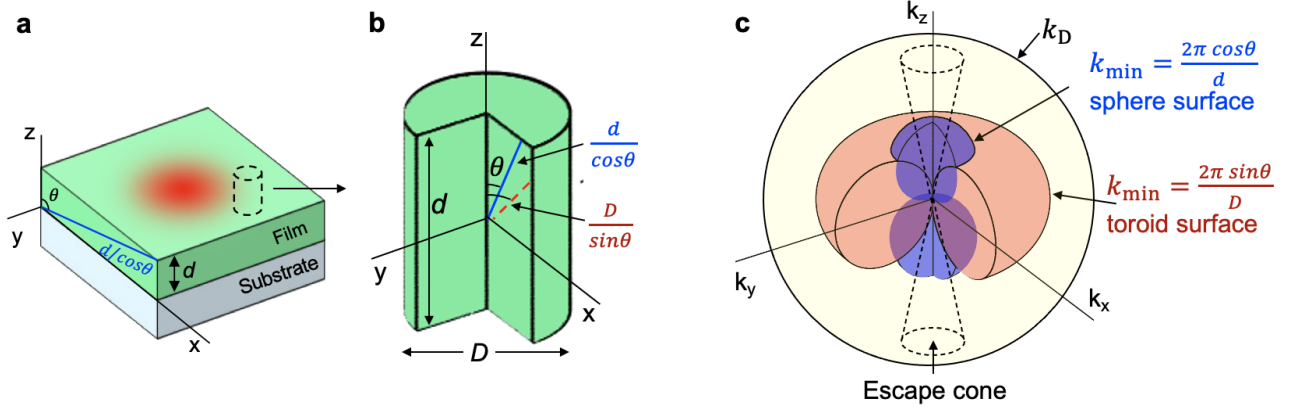


FIG. 1. Model of heat transport under phonon confinement. (a) Real-space schematic of film with thickness d . Film dimensions in the xy plane are much larger than in the z direction (b) Real-space schematic of a cylindrical sample (or nanowire) with height d in the z direction and diameter D in the xy plane. For both, (a) and (b), the angle Θ is measured from the z axis, and rotational symmetry is maintained in the xy plane. (c) The wavevector k -space corresponds to the confined geometries shown in (a) and (b). Confinement imposed by film planes (along the z direction) and by cylinder walls (in the xy plane) prohibits phonon states within blue spheres and a red toroid, respectively, inside the Debye (yellow) sphere. The escape cone is defined by the total internal reflection of phonons at the interface with the substrate according to the acoustic match model [27].

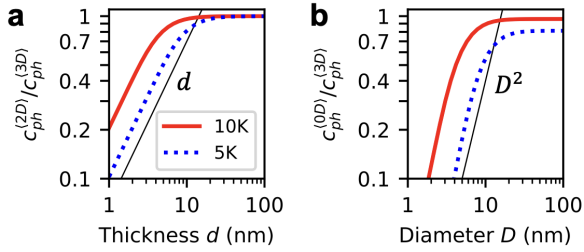


FIG. 2. Reduced phonon heat capacities normalized to the Debye value for confinement imposed by (a) thin film, Eq. (2), and (b) cylinder with a fixed height of 10 nm, Eq. (3). The legend in panel (a) applies to both panels, indicating fixed temperatures. Thin black lines show the expected scaling for the two confined geometries. Material parameters used correspond to those of NbTiN.

B. Phonon escape time

Heat transport between two dissimilar bulk solids was described in [7]. The heat flow per unit area from the film (not indexed) to the substrate (index 0) via phonons (one polarization) is given by

$$\begin{aligned} \frac{dQ}{dt} &= \frac{u}{2} \iint \frac{g(\omega)\hbar\omega}{e^{\hbar\omega/k_B T} - 1} \alpha(\Theta) \sin \Theta \cos \Theta d\omega d\Theta \\ &\quad - \frac{u_0}{2} \iint \frac{g_0(\omega)\hbar\omega}{e^{\hbar\omega/k_B T_0} - 1} \alpha(\Theta_0) \sin \Theta_0 \cos \Theta_0 d\omega d\Theta_0 \\ &= \frac{u}{2} [\mathcal{I}(T) - \mathcal{I}(T_0)]. \end{aligned} \quad (4)$$

Here, $\alpha(\Theta)$ is the phonon transmission coefficient through the interface, given by the acoustic match model [27], which depends on the phonon angle of incidence Θ

and acoustic impedances of the two media. For many solid/solid interfaces, $\alpha(\Theta)$ is constant at small angles and drops to zero at the critical angle of total internal phonon reflection, depicted by the escape cone in Fig. 1c. Phonon states with wavevectors beyond this cone are reflected at the interface and can only escape the film through mechanisms such as inelastic scattering (e.g., absorption and re-emission by electrons) or mode conversion at the interface.

In Eq. (4), since the integrals over frequency are angle-independent, the double integrals $\mathcal{I}(T)$ can be separated. They yield products of the angle-averaged transmission coefficient $\langle \alpha \rangle = 2 \int_0^{\pi/2} \alpha(\Theta) \sin \Theta \cos \Theta d\Theta$ and the phonon energy $U = \frac{1}{2\pi^2} k_B T \left(\frac{k_B T}{\hbar u} \right)^3 \int_0^{x_D} \frac{x^3}{(e^x - 1)} dx$. With the low-temperatures approximation $x_D \rightarrow \infty$, the heat flow becomes $dQ/dt = \frac{\pi^2}{60} \langle \alpha \rangle \frac{k_B^4}{\hbar^3 u^2} (T^4 - T_0^4)$.

Denoting $\Delta T = (T - T_0)$ and assuming small temperature differences $\Delta T \ll (T, T_0)$, the heat flow can be linearized as follows

$$\frac{dQ}{dt} = \frac{u}{2} \frac{d[\mathcal{I}(T)]}{dT} \Delta T. \quad (5)$$

On the other hand, using τ -approximation for small deviations from equilibrium $dx/dt = -x/\tau$ (see e.g. [29] or "correlations of fluctuations in time" in [30]), one can express the heat flow via the rate of energy escape through the interface ($1/\tau_{es}$) as $dQ/dt = (2d c_{ph}/\tau_{es}) \Delta T$. Here, factor 2 appears because the heat flows through only one boundary. By plugging this into Eq. (5), the linearized phonon escape time is given by

$$\tau_{es}^{(3D)} = \frac{4d}{u} \frac{c_{ph}(T)}{d[\mathcal{I}(T)]/dT} = \frac{4d}{\langle \alpha \rangle u}, \quad (6)$$

where for bulk material the derivative $d[\mathcal{I}(T)]/dT = \langle \alpha \rangle c_{ph}(T)$.

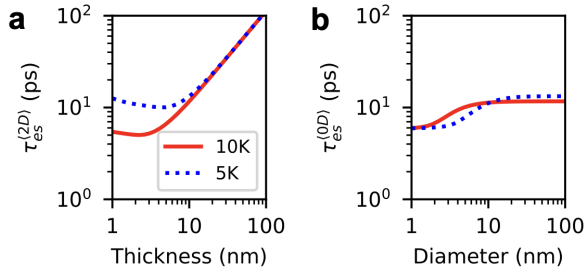


FIG. 3. Modified phonon escape times for confinement imposed by (a) thin film, Eq. (7), and (b) cylinder with a fixed height of 10 nm, Eq. (8). The legend in panel (a) applies to both panels, indicating fixed temperatures. Material parameters used correspond to those of NbTiN/SiO₂.

1. τ_{es} , confinement in thin films

Using the formalism described above, we derive the phonon escape time under confinement in one medium imposed by a thin film, the geometry is shown in Fig. 1a. Only phonon states with wavelengths smaller than $d/\cos\Theta$ (wavevectors $k_{min} = 2\pi \cos\Theta/d$) are present in the film and participate in heat transport, carrying energy out of the film. Their density of states is the Debye DOS $g(\omega)$. Accordingly, this modifies the low-frequency limits of double integrals in Eq. (4).

As evident from Fig. 1c, spheres that prohibit phonon states with k_{min} strongly overlap with the phonon escape cone. Confinement in film reduces the number of phonon states, which could directly escape to the substrate, slowing down heat transport compared to the bulk limit.

The modified phonon escape time (see Appendix A), is given by

$$\tau_{es}^{(2D)} = \frac{4d}{\langle\alpha\rangle u} \frac{c_{ph}^{(2D)}(T, d)}{c_{ph}^{(3D)}(T) [1 - \mu(T, d)]}, \quad (7)$$

where $\mu(T, d) = \frac{15}{4\pi^4} \int_0^{\pi/2} \alpha(\Theta) \sin\Theta \cos\Theta d\Theta \cdot \int_0^{x^*(\Theta)} \frac{x^4 e^x}{(e^x - 1)^2} dx$, and $x^*(\Theta) = 2\pi \cos\Theta/d \cdot \hbar u/k_B T$.

In the bulk limit, $k_{min} \rightarrow 0$ for any Θ , the blue sphere volume $\rightarrow 0$ in Fig. 1c, retrieving the 3D result. In the limit of strong confinement, there are fewer allowed phonon states participating in heat transport which dramatically slows it down. These two limits are seen in Fig. 3a.

2. τ_{es} , confinement in cylinders

Following a similar approach, we derive the phonon escape time for a cylindrical sample, Fig. 1b, where phonons escape through one of the cylinder bases to the substrate. For angles $< \Theta^* = \tan^{-1}(D/d)$, confinement is imposed by cylinder bases (as for the film), and for

angles $> \Theta^*$ by cylinder walls. For simplicity, we ignore phonon scattering at the wall boundaries (see discussion).

The impact of such additional confinement by cylinder walls depends on the ratio between Θ^* and the critical angle of total internal reflection Θ_C (Θ_C defines the escape cone in Fig. 1b). For $\Theta_C < \Theta^*$ the walls prohibit phonon states only beyond the escape cone (otherwise these states could not directly escape the film but via inelastic scattering or mode conversion), speeding up phonon escaping. In the opposite case $\Theta_C > \Theta^*$, cylinder walls do not restrict heat transport and therefore do not affect the escape time. Most likely, however, cylinder diameters do not exceed the film thickness, thus $\Theta^* \leq 45^\circ$, while acoustic impedances of typical nanodevices/substrates result in a wide range of $\Theta_C \geq 30 - 70^\circ$.

The phonon escape time for a cylindrical sample is given by:

$$\tau_{es}^{(0D)} = \frac{4d}{\langle\alpha\rangle u} \frac{c_{ph}^{(0D)}(T, d, D)}{c_{ph}^{(3D)}(T) [1 - \mu(T, d, D)]}, \quad (8)$$

where $\mu(T, d, D) = \frac{15}{4\pi^4} \int_0^{\pi/2} \alpha(\Theta) \sin\Theta \cos\Theta d\Theta \cdot \left[\int_0^{x^*(\Theta)} H_\Theta \frac{x^4 e^x}{(e^x - 1)^2} dx + \int_0^{x^{**}(\Theta)} (1 - H_\Theta) \frac{x^4 e^x}{(e^x - 1)^2} dx \right]$, the upper limits $x^*(\Theta)$ and $x^{**}(\Theta)$ were defined previously. Here H_Θ is a step function, $H_\Theta = 1$ for $\Theta \leq \tan^{-1}(D/d)$ and $H_\Theta = 0$ for $\Theta > \tan^{-1}(D/d)$.

In the limit $D \gg d$, the volume occupied by toroid in k -space (see Fig. 1c) diminishes, and the 2D result is retrieved. In the limit of strong confinement by cylinder walls $D \ll d$, there are fewer phonon states outside the phonon escape cone which speeds up their escaping. These two limiting cases are shown in Fig. 3.

III. RESULTS: COMPARISON WITH EXPERIMENTAL DATA

We applied our model to describe heat transport in strongly disordered NbTiN superconducting devices with the geometry depicted in Fig. 4a.

Heat transport was studied in a *steady state* using the well-established method of self-heating normal domain (see details in Appendix B). To expand the experimental temperature range, we adapted this method to non-zero magnetic fields. Magnetic field reduces the superconducting transition temperature, enabling the heat transport to be studied at lower temperatures. This method involves heating electrons via Joule heat (denoted as P in Fig. 4a), generated by a direct current. The heat flows from electrons to phonons coupled via electron-phonon interaction and then to the thermal bath via phonon escaping to the substrate. We experimentally obtained the overall time required for electron energy to relax from the nanostrip to the substrate τ_E . These times, plotted in Fig. 4b with colored circles, increase with the nanostrip thickness and with lowering the temperature.

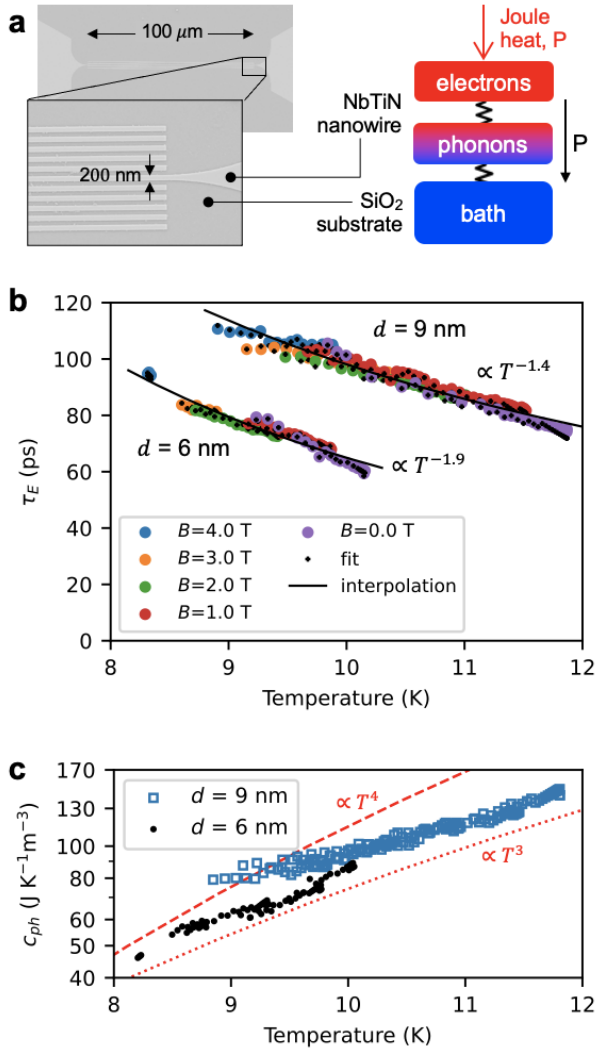


FIG. 4. Experimental analysis of heat transport in NbTiN devices on SiO₂ substrate at low temperatures. (a) Scanning electron microscope images of NbTiN nanostrips, along with schematic heat transport: from electrons within the nanostrip and subsequently to the thermal bath (substrate). (b) Steady-state electron energy relaxation time was obtained for the NbTiN devices with thicknesses $d = 6$ and 9 nm indicated. Experimental data (colored circles) are overlaid with best fits (black dots) obtained with Eq. (9). (c) Phonon heat capacities (markers), computed for confined cylindrical geometry, are reduced to 0.1 times the Debye prediction for bulk material (details are in the main text). The dotted and dashed lines scale as Debye T^3 law and analytic T^4 law for confined thin films, respectively.

The steady-state electron energy relaxation time τ_E is given by the following equation derived from the two-temperature model (for more details see the elaborated model in Ref.[31]):

$$\tau_E(T_e) = \tau_{EP}(T_e) + \gamma(c_e(T_e)/c_{ph}(T_{ph}))\tau_{es} \quad (9)$$

Here, T_e and T_{ph} denote the effective temperatures of electrons and phonons, respectively, c_e and c_{ph} denote

their heat capacities, and γ is about one (see Appendix). The electron-phonon interaction time τ_{EP} in thin disordered NbTiN films scales as T^{-n} with $n = 3.4 - 3.5$, ranging from 5 to 1 ps over the temperature range of 8 - 12 K [32].

To fit the experimental $\tau_E(T)$ data, we used known NbTiN material parameters[32], such as c_e and τ_{EP} , while the phonon heat capacity c_{ph} and escape time τ_{es} were computed with our model accounting for three phonon polarizations. Given the level of disorder in granular NbTiN films [32], which likely impacts the shear modulus [33, 34], we treated the transverse sound velocity as a fitting parameter. Optimal agreement with experimental data was only achieved by assuming confinement in all three directions, i.e., confined cylindrical geometry. Using c_{ph} and τ_{es} computed for 3D bulk phonons, as well as for phonons confined in a film, resulted in relaxation time values that were underestimated, by at least a factor of four, compared to the experimental values. The cylindrical geometry is likely due to the polycrystalline granular morphology of NbTiN films, where crystalline grains (nanometric cylinders) are embedded in an amorphous environment [35]. A similar dense columnar granular morphology has been reported in thicker NbTiN films [36].

The best-fit relaxation times are plotted in Fig. 4b, with black dots. These were obtained with sound velocities reduced to $0.94 \pm 4.4\%$ and $0.95 \pm 7.1\%$ times the bulk transverse sound velocity of 4700 m/s [37] for the 6 and 9 nm-thick strips, respectively. The reduced velocities are consistent with the structural difference between a bulk monocrystal and an aggregate of crystalline grains at the nanoscale, since structural disorder always reduces the shear modulus (compared to the corresponding perfect crystal) due to nonaffine displacements [33]. The longitudinal velocity was fixed to 8400 m/s, the same as in the bulk material[37], consistent with the well-known fact that the compression modulus is less affected by disorder and nonaffinity [38]. We also varied the cylinder diameter (D), while fixing its height to equal the film thickness. The best-fit diameter for both devices was 1.72 nm, containing at least four elementary cells along the confined direction. Strictly, this low number of elementary cells requires replacing integration with summation over allowed modes. However, for the sake of the self-consistency of our model, we keep using integral representation for all geometries. Moreover, given the unknown cross-sectional shapes of columnar grains, the distribution of their sizes, and the packing density, our best-fit value should not be considered as a physical grain diameter.

Using these parameters, we computed phonon heat capacities with Eq. (3), which are plotted in Fig. 4c (markers). They are significantly reduced, ≈ 0.1 times the Debye prediction for 3D bulk material, and exhibit a clear dependence on film thickness. For reference, Fig. 4c shows the Debye T^3 scaling (dotted line) and the analytical T^4 law (dashed line, Eq. (A1)) for confined thin films [21], leaving the discussion of the temperature de-

pendence of heat capacity outside the scope of this work. We also computed phonon escape times with Eq. (8), obtaining values of $\tau_{es} = 4.2 \pm 2.1\%$ ps and $6.1 \pm 4.2\%$ ps for the 6 and 9 nm-thick devices, respectively. According to Eq. (9), these escape times, along with large c_e/c_{ph} ratios (due to strongly reduced c_{ph}), lead to large energy relaxation times τ_E . The computed τ_{es} scale linearly with thickness as $\approx 0.7d$ and are slightly smaller compared to what is expected in the bulk limit, $\approx 1.1d$ (the film/substrate interface transmission coefficient is ≈ 0.7). The difference is due to the confinement effect imposed by cylinder walls.

IV. DISCUSSION

Below we evaluate the implications of our findings on phonon mode confinement and discuss how these insights can advance the understanding and performance of nanodevices at low temperatures.

Validation of the Heat Transport Model

Our heat transport model describes the effect of confinement imposed by the geometry of nanostructures on phonon modes. The reduction in allowed phonon modes not only (i) reduces phonon heat capacities and (ii) modifies phonon escape time but also (iii) significantly slows down electron energy relaxation (overall electron cooling), as demonstrated through our application of the two-temperature model via Eq. (9).

Experiments on NbTiN devices support our assumption that phonon modes are confined within polycrystalline columnar grains resembling cylinders. The overall cylinder sizes of a few nanometers are comparable to phonon mean-free paths. In this case, as shown in [23], the rate of heat removal is not governed by reflections at the grain boundaries (cylinder walls), but rather by the electron-phonon interactions within grains.

Our model is based on the assumption that low-frequency (long-wavelength) phonons do not contribute to heat transport due to confinement effects. This assumption is unequivocally valid when the confined medium interfaces with a vacuum. However, when it interfaces with another solid, such as a substrate, the vibrational wave can extend into the substrate despite acoustic mismatch at the interface. Consequently, the criteria for determining the low-frequency cutoff become less clear. It is even less defined when phonon modes are confined within crystalline granules of polycrystalline films, where the grain boundaries are often thinner than the phonon wavelength. Addressing this issue comprehensively would greatly complicate our heat transport model, shifting the focus from its convenient practical application. However, we speculate that our simplified model remains valid because the grain boundaries are

likely oxidized, and the grain sizes serve as an adjustable parameter.

Effects shown in moderately disordered 2D graphene [24–26], such as impurity-enhanced electron-phonon scattering and temperature profile asymmetries near defects, should also be present in our NbTiN devices, but they do not impact our results. Our devices are strongly disordered, where impurities are densely and uniformly distributed over a distance of a few nanometers. In our experiments with self-heating normal domains with lengths of tens of micrometers, measured heat transport is dominated by the central domain region, rather than by non-trivial scattering effects around narrow domain walls.

Implications for Nanodevices

The effect of confined phonon modes can significantly enhance the performance of SNSPDs. As confinement increases, c_{ph} decreases, resulting in higher sensitivity to low-energy photons. This sensitivity enhancement is due to the increased fraction of photon energy transferred to the electron system, $\propto c_e/(c_e + c_{ph})$ [39]. Additionally, smaller c_{ph} reduces thermal noise, caused by thermal fluctuations in electron energy, by decreasing the variance of electron energy fluctuations, in full accordance with statistical thermodynamics [40]. This might play a key role in minimizing the dark count rate in SNSPDs [41], improving their ability to detect extremely low and rare events like dark matter particles [42], and enhancing timing accuracy (timing jitter) critical in laser ranging applications.

The performance of Hot Electron Bolometers (HEBs) [43], employed in terahertz spectroscopy, also benefits from these adjustments in thermal properties. The responsivity of HEB-mixers is a key metric in their numeric calibration and is directly affected by the c_e/c_{ph} ratio. Any inaccuracies in defining this ratio eventually lead to calibration errors. For example, in atomic oxygen spectroscopy with HEB [44], which plays an important role in the chemistry and energy balance of the earth's atmosphere, any calibration errors can skew the forecast for climate change.

Such devices for hybrid electronics as thermal switches (nanocryotrons), which rely on superconducting nanowires [45, 46] see variations in the heating/switching device operation due to changes in thermal properties induced by confinement. For example, slowed-down electron energy relaxation leads to smaller dissipated heat (heating currents) and slower switching dynamics.

A way to control confinement is the reduction of the device dimensions as in films, wires, or grains. For instance, the discussed performance enhancements are readily achievable in SNSPDs based on amorphous superconductors like MoSi and WSi by reducing the film thickness. In polycrystalline materials such as NbN and NbTiN, reduction in the grain size by adjusting the sputtering conditions (e.g. ambient substrate temperature

and gas flow [47]) can similarly improve device metrics.

V. CONCLUSION

In this study, we developed and validated a computational model of phonon-mediated heat transport under confinement in nanostructures at low temperatures. Our findings reveal that confinement significantly reduces phonon heat capacities and slows down electron cooling to the substrate, which aligns with the granular morphology of the studied NbTiN nanostructures.

These insights pave the way for future advances in the design and performance of cryogenic nanodevices through tailored microstructure engineering. Notably, the increased infrared sensitivity of superconducting single-photon detectors and improved accuracy in thermal management in Hot Electron Bolometers would significantly impact quantum computing and atmospheric science.

ACKNOWLEDGMENT

The authors greatly acknowledge V. Zwiller for his help in the device preparation, A. Sergeev for his essential insights regarding the impact of the magnetic field on electron-phonon interaction, as well as A. I. Bezuglyj for the fruitful discussion on phonon confinement. M.S. acknowledges funding support from the National Research Foundation, Singapore and A*STAR under the Quantum Engineering Programme (QEP-P1). A.Z. gratefully acknowledges funding from the European Union through Horizon Europe ERC Grant number: 101043968 “Multi-mech”, and from US Army Research Office through contract nr. W911NF-22-2-0256.

Appendix A: Confinement of phonon modes

The confinement model, described in the main text, uses Debye DOS and integration over an angle-dependent wavevector (see e.g., Eq. (2)). Alternatively, one can introduce the confinement effect on the DOS using the approach of [8].

The total number of states is found as the ratio of the volume in k -space, $\delta V_k = 2 \int_0^{2\pi} d\phi \int_0^{\pi/2} d\Theta \sin \Theta k^2 dk$ (performing the angular integrals gives 4π), to the volume occupied by a single state, $(2\pi)^3/V$, that is $N = V/(2\pi^2)k^2 dk$. And the Debye density of states (per unit volume) is simply $g(k) = dN/dk = k^2/2\pi^2$. Under confinement imposed by film planes, the minimum allowed wavevector depends on the polar angle as $k_{min} = 2\pi \cos \Theta/d$, which modifies the volume in k -space as follows $\delta V_k^* = 2 \int_0^{2\pi} d\phi \int_{\arccos(kd/2\pi)}^{\pi/2} d\Theta \sin \Theta k^2 dk = 2dk^3 dk$. The modified DOS (per unit volume) is then $g^*(k) = k^3 d/4\pi^3$ [8].

One then can express phonon heat capacity (per mode) as a sum of capacities with the modified DOS within a sphere of radius $k^* = 2\pi/d$ and with the Debye DOS within a spherical shell extending from k^* to the Debye wavevector k_D :

$$c_{ph}^{(2D)}(T, d) = \frac{d}{4\pi^3} k_B \left(\frac{k_B T}{\hbar u} \right)^4 \int_0^{x^*} \frac{x^5 e^x}{(e^x - 1)^2} dx + \frac{1}{2\pi^2} k_B \left(\frac{k_B T}{\hbar u} \right)^3 \int_{x^*}^{x_D} \frac{x^4 e^x}{(e^x - 1)^2} dx, \quad (A1)$$

where $x^* = 2\pi\hbar u/dk_B T$. In the limit of strong confinement, $x^* \rightarrow x_D$, the second term diminishes, and $c_{ph} = 120\zeta(5) \frac{d}{4\pi^3} k_B \left(\frac{k_B T}{\hbar u} \right)^4 \propto T^4 d$ with the Riemann zeta function ζ .

When deriving phonon escape time under confinement imposed by thin film, the heat flow integrals are modified as follows:

$$\mathcal{I}^{(2D)}(T) = \int_0^{\pi/2} \alpha(\Theta) \sin \Theta \cos \Theta \times \int_{\omega^*(\Theta)}^{\omega_D} \frac{g(\omega) \hbar \omega}{e^{\hbar \omega/k_B T} - 1} d\omega d\Theta, \quad (A2)$$

where, $\omega^*(\Theta) = u 2\pi \cos \Theta/d$. For a given direction of phonon propagation defined by the angle Θ , only phonons with wavevectors $k > 2\pi \cos \Theta/d$ (wavelengths $< d/\cos \Theta$) are present in the film and may carry the energy out of the film; they have the Debye DOS $g(\omega)$. The derivative of the heat flow integral over temperature is given by:

$$\frac{d[\mathcal{I}^{(2D)}(T)]}{dT} = \frac{1}{2\pi^2} k_B \left(\frac{k_B T}{\hbar u} \right)^3 \times \int_0^{\pi/2} \alpha(\Theta) \sin \Theta \cos \Theta \int_{x^*(\Theta)}^{x_D} \frac{x^4 e^x}{(e^x - 1)^2} dx d\Theta = \langle \alpha \rangle c_{ph}^{(3D)}(T) \left[1 - \mu(T, d) \right], \quad (A3)$$

where, $x^*(\Theta)$ and $\mu(T, d)$ were defined in the main text. The integral in Eq. (A3) are expressed as a difference $\int_{x^*(\Theta)}^{x_D} dx = \left[\int_0^{x_D} dx - \int_0^{x^*(\Theta)} dx \right]$. Finally, the escape time is modified to Eq. (7).

Finally, to describe the experimental data we accounted for all three polarizations (two transversal and one longitudinal) and used the weighted time

$$\tau_{es} = \left[\frac{\sum_i \tau_{es,i}^{-1} c_{ph,i}}{\sum_i c_{ph,i}} \right]^{-1}. \quad (A4)$$

Here the decay rate of each phonon polarisation $\tau_{es,i}^{-1}$ is weighed by its corresponding heat capacity $c_{ph,i}$. This ensures that the contribution of each polarisation to the overall heat transport is proportionate to its ability to store thermal energy. We also note that the acoustic match model[27], which we used to compute the transmission coefficient $\langle \alpha \rangle$, accounts for mode conversion.

Appendix B: Self-heating normal domain in magnetic field

The self-heating normal domain (SHND) technique is an established method[48–51] for studying heat transport in superconducting strips. It is done by creating a steady-state normal domain in a superconducting strip heated by a hysteresis current at temperatures above the transition temperature T_C . We extended this technique for non-zero magnetic field to expand the experimental temperature range beyond T_C . Below, we provide experimental details and reasoning why the formalism, which we developed in detail in Ref.[51] for zero magnetic field is valid for non-zero fields. For mathematical details we refer to Ref.[51].

We studied heat transport in thin NbTiN nanostrips at temperatures below 12 K. Measurements were conducted in physical property measurement system in magnetic fields ranging from 0 T to 4 T applied perpendicular to the substrate plane as sketched in Fig. 5a. The studied NbTiN strips with thicknesses $d = 6$ nm and 9 nm, widths $w = 200$ nm, and lengths $l = 100$ μm , were fabricated on Si substrates above 270 nm-thick thermally grown SiO_2 buffer layers (properties of these NbTiN films were reported in [32]).

Figure 5c shows typical hysteretic current-voltage (IV) curves of a superconducting nanostrip in zero magnetic field $B = 0$ (dashed curve) as well as in a non-zero field of 1 T (solid curve). Sweeping the current from the above critical (switching) value I_C downwards makes the nanostrip to return from the normal to the superconducting state through a resistive plateau defined by the hysteresis (return or retrapping) current I_r . This plateau corresponds to a self-heating normal domain with a length proportional to the voltage. External magnetic field reduces both currents, I_C and I_r , as depicted by the solid curve in Fig. 5c. It also suppresses the T_C (inset in Fig. 5c). We note here that the measured $I_r(B = 0)$ for the 9 nm-thick strip is consistent with values reported earlier for similar 10 nm-thick NbTiN films [52] (see also a comment [53]).

Figure 5d,e, shows $I_r(T_B, B)$ dependencies, which were extracted from IV curves measured at different bath temperatures, T_{bath} , and preset magnetic fields. In our experiment, the applied magnetic fields drive the superconducting strip into a mixed vortex state. This state emerges between the upper-critical field $B_{c2}(T = 0) > 13.9$ T (estimated based in data in [32]) and the field $B_C \approx 0.2$ T at which a transition from the vortex-free Meissner to mixed vortex state occurs (estimated according to the Ginzburg–Landau model [54] and consistent with values reported for similar NbTiN films [55]). Screening currents induced by a non-zero magnetic field sum up with the transport current, resulting in non-uniform net current density across the superconducting part of the strip as illustrated in Fig. 5b with current lines. Although this may alter the shape of normal domain edges (sketched in Fig. 5b in red), for large domains,

the translational symmetry (space homogeneity) with respect to domain edges dictates that the edges and the mixed vortex state of superconducting parts of the strip do not affect the temperature at the domain center (T_{e0}). For sufficiently large domains, the finite temperature at the domain center requires the derivative $\partial^2 T / \partial x^2$ at the center to approach zero. These conditions allow us to apply the SHND formalism, developed [51] for $B = 0$, to the non-zero fields.

In the SHND model, the hysteresis current is given by

$$I_r = \sqrt{\frac{c_e(T_e)w^2d}{p\tau_E(T_e)R_{\square}T_e^{p-1}}(T_e^p - T_B^p)}, \quad (\text{B1})$$

where T_e , c_e , and R_{\square} are the electron temperature in the domain center, the volumetric heat capacity of electrons, and the sheet resistance of the film, respectively. The steady-state time of electron energy relaxation to the substrate $\tau_E(T_e) \approx \tau_{EP}(T_e) + \tau_{es}c_e(T_e)/c_{ph}(T_{ph})$ is given by the advanced two-temperature model[31], which is similar to the conventional model[56]. Here, τ_{es} is the phonon escape time, and τ_{EP} is the electron-phonon (e - ph) interaction time, T_{ph} , is the phonon temperature in the domain center.

To validate the use of Eq. (B1) for the evaluation of the experimental data at non-zero magnetic field, we first estimate the field impact on the parameters entering this equation. Magnetic field separates the electron states with opposite spin directions by the Zeeman splitting energy $2\mu_B B$ (μ_B is the Bohr magneton) that affects the electron density of states $D(E)$ and, consequently, the electron heat capacity $c_e = \int D(E)f_{FD}(E)EdE$ (here $f_{FD}(E)$ is the Fermi-Dirac distribution function). The correction to the electron heat capacity is of the order of $(\mu_B B/E_F)^2/8$ where E_F is the Fermi energy. For fields used in our experiment, the splitting energy (< 0.5 meV) is much smaller than the Fermi energy (≈ 5 eV), and therefore the effect of splitting on $D(E)$ and c_e is negligible. Furthermore, it is clear that magnetic field has no direct impact on the number of phonons and, therefore, no effect on c_{ph} and τ_{es} .

Now let us consider possible field effects on τ_{EP} . In a non-magnetic and non-piezoelectric normal metal, magnetic field can affect the e - ph coupling via screening of electromagnetic interaction between electrons and vibrating ions of the crystalline lattice and via induced changes in the deformation potential. The effect through both channels is parameterized with the frequency-dependent conductivity tensor [57]. The direct electromagnetic interaction is completely screened in our case, since, for $T_{ph} = 10$ K, frequencies of thermal acoustic phonons $\omega_T/(2\pi) \approx 2 \cdot 10^{11}$ Hz are much less than the plasma frequency $\omega_p/(2\pi) \approx 4 \cdot 10^{15}$ Hz and the characteristic frequency $\sigma^{-1}\varepsilon_0\varepsilon_r/(2\pi) \approx 2 \cdot 10^{15}$ Hz (σ and ε_r are the dc conductivity and the dielectric permittivity at infinite frequency, respectively) above which the conductivity becomes frequency dependent. On the other hand, the applied magnetic fields are not strong enough

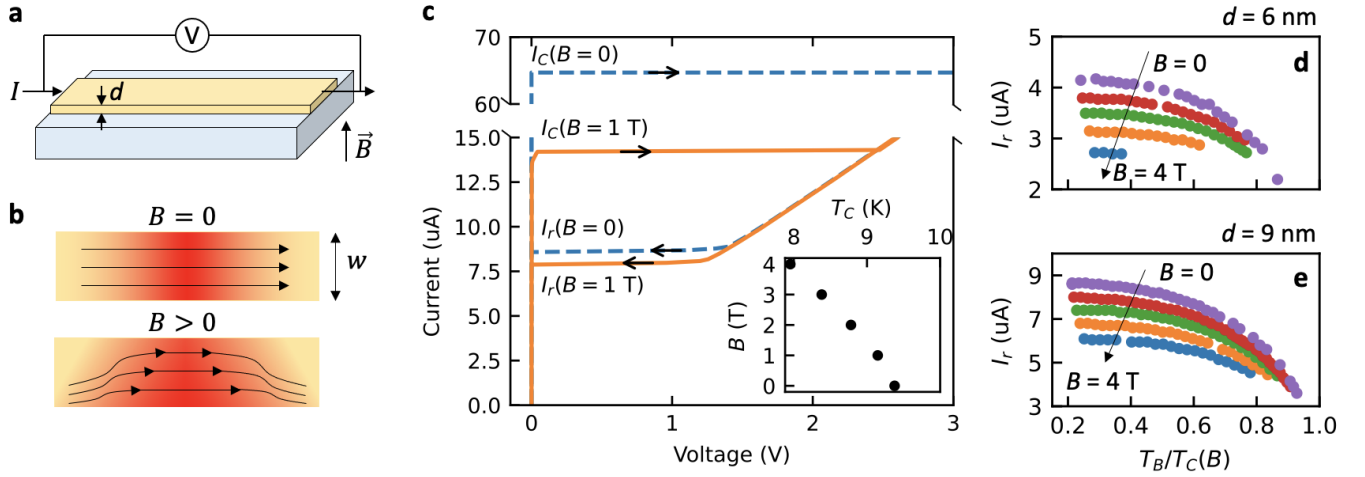


FIG. 5. (a) Schematic of self-heating domain experiment in external magnetic field B . (b) Schematics of the magnetic field effect on the current density (indicated by current lines) and on the domain shape (shown in red). (c) IV curves measured at the bath temperature $T_{bath} = 2.4$ K with ($B = 1$ T, solid line) and without ($B = 0$, dashed line) magnetic field for the 9 nm-thick strip. Arrows indicate the sweep direction of the current. I_C and I_r are the critical (switching) and hysteresis (return or retrapping) currents. Inset: Field-dependent transition temperature. (d) and (e) Experimental hysteresis currents at preset magnetic fields ($B = 0, 1, 2, 3$, and 4 T) vs. bath temperatures (T_{bath}) normalized with field-dependent transition temperatures $T_C(B)$ for strips with thicknesses $d = 6$ and 9 nm, respectively.

to cause cyclotron resonance (Landau quantization). Indeed, in our case the cyclotron frequency $\omega_c = eB/m_e$ ($\omega_c/(2\pi) \approx 1.1 \cdot 10^{11}$ Hz for $B = 4$ T) is much smaller than the reciprocal elastic scattering time $\tau \approx 1$ fs [32]. Under these conditions, electrons do not complete at least one entire orbit without being scattered and, consequently, cannot experience a resonance-energy exchange with thermal phonons. Corrections to the diagonal elements in the conductivity tensor [58] are of the order $(\omega_c\tau)^2 \approx 1.5 \cdot 10^{-6}$ and can be safely neglected. Finally, since all the discussed material parameters do not depend on the magnetic field, the exponent p in Eq. (B1) is likewise field-independent (in a particular film p is determined by the phonon dimensionality and the degree of disorder [29]).

Assuming field-independent material parameters, the experimental $I_r(T_B, B)$ data, shown in Fig. 5(d,e), were fitted with Eq. (B1). The temperatures T_e and T_{ph} were found for each pair of values B and T_{bath} . Other material parameters for our films were taken from Ref.[32]. We used τ_E and p as the only field-independent fitting parameters. The fit was subject to an additional restriction: τ_E to be a smooth function (power law) of temperature. The best-fit $\tau_E(T_e)$ obtained with the least-squares method are shown in Fig. 4a.

Best-fit values of exponents $p = 4.2$ and 3.6 were found for strips with thicknesses $d = 6$ nm and 9 nm, respectively. Fitting $\tau_E(T_e)$ data with a power law (solid curves in Fig. 4a) results in dependences $\tau_E \propto T^{-1.9}$ for the 6 nm-thick film and $\tau_e \propto T^{-1.4}$ for the 9 nm-thick film.

[1] S. D. Bass and M. Doser, Quantum sensing for particle physics, *Nature Reviews Physics*, 1 (2024).
 [2] I. Esmail Zadeh, J. Chang, J. W. Los, S. Gyger, A. W. Elshaari, S. Steinhauer, S. N. Dorenbos, and V. Zwiller, Superconducting nanowire single-photon detectors: A perspective on evolution, state-of-the-art, future developments, and applications, *Applied Physics Letters* **118** (2021).
 [3] M. H. Devoret and R. J. Schoelkopf, Superconducting circuits for quantum information: an outlook, *Science* **339**, 1169 (2013).
 [4] A. I. Braginski, Superconductor electronics: Status and outlook, *Journal of superconductivity and novel magnetism* **32**, 23 (2019).
 [5] B. G. Oripov, D. S. Rampini, J. Allmaras, M. D. Shaw, S. W. Nam, B. Korzh, and A. N. McCaughan, A super-

conducting nanowire single-photon camera with 400,000 pixels, *Nature* **622**, 730 (2023).
 [6] S. K. Tolpygo, Superconductor digital electronics: Scalability and energy efficiency issues, *Low Temperature Physics* **42**, 361 (2016).
 [7] W. Little, The transport of heat between dissimilar solids at low temperatures, *Canadian Journal of Physics* **37**, 334 (1959).
 [8] Y. Yu, C. Yang, M. Baggioli, A. E. Phillips, A. Zacccone, L. Zhang, R. Kajimoto, M. Nakamura, D. Yu, and L. Hong, The ω^3 scaling of the vibrational density of states in quasi-2d nanoconfined solids, *Nature Communications* **13**, 3649 (2022).
 [9] M. C. Wingert, Z. C. Chen, E. Dechaumphai, J. Moon, J.-H. Kim, J. Xiang, and R. Chen, Thermal conductivity of ge and ge-si core-shell nanowires in the phonon

- confinement regime, *Nano letters* **11**, 5507 (2011).
- [10] V. Novotny, P. Meincke, and J. Watson, Effect of size and surface on the specific heat of small lead particles, *Physical Review Letters* **28**, 901 (1972).
 - [11] D. Halbertal, J. Cuppens, M. B. Shalom, L. Embon, N. Shadmi, Y. Anahory, H. Naren, J. Sarkar, A. Uri, Y. Ronen, *et al.*, Nanoscale thermal imaging of dissipation in quantum systems, *Nature* **539**, 407 (2016).
 - [12] D. Halbertal, M. Ben Shalom, A. Uri, K. Bagani, A. Y. Meltzer, I. Marcus, Y. Myasoedov, J. Birkbeck, L. S. Levitov, A. K. Geim, *et al.*, Imaging resonant dissipation from individual atomic defects in graphene, *Science* **358**, 1303 (2017).
 - [13] H. P. Baltes and E. Hilf, Specific heat of lead grains, *Solid State Communications* **12**, 369 (1973).
 - [14] R. Lautenschläger, Improved theory of the vibrational specific heat of lead grains, *Solid State Communications* **16**, 1331 (1975).
 - [15] R. Prasher and P. Phelan, Non-dimensional size effects on the thermodynamic properties of solids, *International journal of heat and mass transfer* **42**, 1991 (1999).
 - [16] A. J. McNamara, B. J. Lee, and Z. M. Zhang, Quantum size effect on the lattice specific heat of nanostructures, *Nanoscale and Microscale Thermophysical Engineering* **14**, 1 (2010), <https://doi.org/10.1080/15567260903468612>.
 - [17] A. E. Phillips, M. Baggioli, T. W. Sirk, K. Trachenko, and A. Zaccone, Universal 1-3 finite-size effects in the viscoelasticity of amorphous systems, *Physical Review Materials* **5**, 035602 (2021).
 - [18] A. Zaccone and K. Trachenko, Explaining the low-frequency shear elasticity of confined liquids, *Proceedings of the National Academy of Sciences* **117**, 19653 (2020), <https://www.pnas.org/doi/pdf/10.1073/pnas.2010787117>.
 - [19] H. Yang, G. Ji, M. Choi, S. Park, H. An, H.-T. Lee, J. Jeong, Y. D. Park, K. Kim, N. Park, J. Jeong, D.-S. Kim, and H.-R. Park, Suppressed terahertz dynamics of water confined in nanometer gaps, *Science Advances* **10**, eadm7315 (2024), <https://www.science.org/doi/pdf/10.1126/sciadv.adm7315>.
 - [20] A. Zaccone, Explaining the thickness-dependent dielectric permittivity of thin films, *Phys. Rev. B* **109**, 115435 (2024).
 - [21] A. Zaccone, Quantum confinement theory of the heat capacity of thin films, *Phys. Rev. Mater.* **8**, 056001 (2024).
 - [22] In Ref.[21], the analysis initially showed good agreement between experimental heat capacity data from our lab and the analytical T^4d law for thin films. However, later we revealed discrepancies, as the heat capacities were indirectly derived from electron cooling times using the two-temperature model. In particular, the original analysis overlooked the confinement effect on electron cooling. By incorporating this effect, we achieved quantitative consistency with experimental data, assuming tree-dimensional confinement in grains as detailed in the present paper.
 - [23] A. Bezuglyj and L. Davydov, Phonon heat removal from metal nano-particles and dynamics of nano-particle cooling at low temperatures, *New Journal of Physics* (2024).
 - [24] J. F. Kong, L. Levitov, D. Halbertal, and E. Zeldov, Resonant electron-lattice cooling in graphene, *Physical Review B* **97**, 245416 (2018).
 - [25] K. Tikhonov, I. Gornyi, V. Y. Kachorovskii, and A. Mirlin, Asymmetry of nonlocal dissipation: From drift-diffusion to hydrodynamics, *Physical Review B* **100**, 205430 (2019).
 - [26] N. G. Leumer, D. M. Basko, R. A. Jalabert, D. Weinmann, and R. S. Whitney, Going beyond landauer scattering theory to describe spatially-resolved non-local heating and cooling in quantum thermoelectrics, *arXiv preprint arXiv:2407.10192* (2024).
 - [27] S. B. Kaplan, Acoustic matching of superconducting films to substrates, *Journal of Low Temperature Physics* **37**, 343 (1979).
 - [28] R. Travaglini and A. Zaccone, Analytical theory of enhanced bose-einstein condensation in thin films, *Journal of Physics B: Atomic, Molecular and Optical Physics* **55**, 055301 (2022).
 - [29] A. Bezuglyi and V. Shklovskii, The kinetics of low-temperature electron-phonon relaxation in a metallic film following instantaneous heating of the electrons, *Journal of Experimental and Theoretical Physics* **84**, 1149 (1997).
 - [30] L. D. Landau and E. M. Lifshitz, *Statistical Physics: Volume 5*, Vol. 5 (Elsevier, 2013).
 - [31] A. D. Semenov, M. Wienold, M. Sidorova, and H.-W. Hübers, Analytical correction for direct detection in the retrieval of gas spectral lines measured with superconducting hot-electron bolometer mixer, *Journal of Applied Physics* **135**, 134502 (2024), <https://pubs.aip.org/aip/jap/article-pdf/doi/10.1063/5.0189111/19866103/134502.1.5.0189111.pdf>.
 - [32] M. Sidorova, A. Semenov, H.-W. Hübers, S. Gyger, S. Steinhauer, X. Zhang, and A. Schilling, Magnetoconductance and photoresponse properties of disordered NbTiN films, *Physical review B* **104**, 184514 (2021).
 - [33] A. Zaccone and E. Scossa-Romano, Approximate analytical description of the nonaffine response of amorphous solids, *Phys. Rev. B* **83**, 184205 (2011).
 - [34] M. Krief and Y. Ashkenazy, Spatial distribution of local elastic moduli in nanocrystalline metals, *Physical Review Research* **6**, 023253 (2024).
 - [35] J. Zichi, J. Chang, S. Steinhauer, K. von Fieandt, J. W. N. Los, G. Visser, N. Kalhor, T. Lettner, A. W. Elshaari, I. E. Zadeh, and V. Zwiller, Optimizing the stoichiometry of ultrathin nbtin films for high-performance superconducting nanowire single-photon detectors, *Opt. Express* **27**, 26579 (2019).
 - [36] A. Karimi, D. La Grange, N. Goebbels, and A. Santana, Structural and mechanical properties of nb1-x tixn thin films deposited by rf magnetron sputtering, *Thin Solid Films* **607**, 14 (2016).
 - [37] M. Arockiasamy, M. Sundareswari, and M. Rajagopalan, Ductility behaviour of cubic titanium niobium nitride ternary alloy: a first-principles study, *Indian Journal of Physics* **90**, 149 (2016).
 - [38] A. Zaccone, *Theory of Disordered Solids* (Springer, Cham, 2023).
 - [39] D. Y. Vodolazov, Single-photon detection by a dirty current-carrying superconducting strip based on the kinetic-equation approach, *Phys. Rev. Appl.* **7**, 034014 (2017).
 - [40] J. Hajdu, R. balescu: Equilibrium and nonequilibrium statistical mechanics. john wiley & sons, chichester, new york, sydney, toronto 1975, 742 seiten, preis:£ 16.20. (1977).
 - [41] A. D. Semenov, M. Sidorova, M. A. Skvortsov, A. Kuzmin, K. Ilin, and M. Siegel, Local thermal fluctuations in current-carrying superconducting nanowires,

- Physical Review B **102**, 184508 (2020).
- [42] J. Chiles, I. Charaev, R. Lasenby, M. Baryakhtar, J. Huang, A. Roshko, G. Burton, M. Colangelo, K. Van Tilburg, A. Arvanitaki, *et al.*, New constraints on dark photon dark matter with superconducting nanowire detectors in an optical haloscope, *Physical Review Letters* **128**, 231802 (2022).
 - [43] J. J. A. Baselmans, A. Baryshev, S. F. Reker, M. Hajenius, J. R. Gao, T. M. Klapwijk, B. Voronov, and G. Gol'tsman, Influence of the direct response on the heterodyne sensitivity of hot electron bolometer mixers, *Journal of Applied Physics* **100**, 084510 (2006).
 - [44] H. Richter, C. Buchbender, R. Higgins, B. Klein, J. Stutzki, H. Wiesemeyer, and H.-W. Hübers, Direct measurements of atomic oxygen in the mesosphere and lower thermosphere using terahertz heterodyne spectroscopy, *Communications Earth and Environment* **2**, 19 (2021).
 - [45] A. N. McCaughan and K. K. Berggren, A superconducting-nanowire three-terminal electrothermal device, *Nano letters* **14**, 5748 (2014).
 - [46] R. Baghdadi, J. P. Allmaras, B. A. Butters, A. E. Dane, S. Iqbal, A. N. McCaughan, E. A. Toomey, Q.-Y. Zhao, A. G. Kozorezov, and K. K. Berggren, Multilayered heater nanocryotron: A superconducting-nanowire-based thermal switch, *Physical Review Applied* **14**, 054011 (2020).
 - [47] A. E. Dane, A. N. McCaughan, D. Zhu, Q. Zhao, C.-S. Kim, N. Calandri, A. Agarwal, F. Bellei, and K. K. Berggren, Bias sputtered NbN and superconducting nanowire devices, *Applied Physics Letters* **111**, 122601 (2017).
 - [48] W. Skocpol, M. Beasley, and M. Tinkham, Self-heating hotspots in superconducting thin-film microbridges, *Journal of Applied Physics* **45**, 4054 (1974).
 - [49] A. Dane, J. Allmaras, D. Zhu, M. Onen, M. Colangelo, R. Baghdadi, J.-L. Tambasco, Y. Morimoto, I. E. Forno, I. Charaev, *et al.*, Self-heating hotspots in superconducting nanowires cooled by phonon black-body radiation, *Nature Communications* **13**, 5429 (2022).
 - [50] S. Yamasaki and T. Aomine, Self-heating effects in long superconducting thin films over a wide temperature range, *Japanese Journal of Applied Physics* **18**, 667 (1979).
 - [51] M. Sidorova, A. D. Semenov, H.-W. Hübers, S. Gyger, and S. Steinhauer, Phonon heat capacity and self-heating normal domains in NbTiN nanostrips, *Superconductor Science and Technology* **35**, 105005 (2022).
 - [52] S. Steinhauer, L. Yang, S. Gyger, T. Lettner, C. Errando-Herranz, K. D. Jöns, M. A. Baghban, K. Gallo, J. Zichi, and V. Zwiller, Nbtin thin films for superconducting photon detectors on photonic and two-dimensional materials, *Applied Physics Letters* **116**, 171101 (2020).
 - [53] In [52], the authors reported the effect of the substrate on the hysteresis (retrapping) current. We attribute it to variations in the acoustic matching between the film and the substrate. Specifically, improved acoustic matching enhances cooling efficiency, which requires more power to be dissipated to maintain a normal operation in the steady state, as a result, a larger hysteresis current is required.
 - [54] G. M. Maksimova, N. V. Zhelezina, and I. L. Maksimov, Critical current and negative magnetoresistance of superconducting film with edge barrier, *Europhysics Letters* **53**, 639 (2001).
 - [55] M. Jönsson, R. Vedin, S. Gyger, J. A. Sutton, S. Steinhauer, V. Zwiller, M. Wallin, and J. Lidmar, Current crowding in nanoscale superconductors within the ginzburg-landau model, *Physical Review Applied* **17**, 064046 (2022).
 - [56] N. Perrin and C. Vanneste, Response of superconducting films to a periodic optical irradiation, *Physical Review B* **28**, 5150 (1983).
 - [57] H. N. Spector, Interaction of acoustic waves and conduction electrons (Academic Press, 1967) pp. 291–361.
 - [58] A. A. Abrikosov, *Fundamentals of the Theory of Metals* (Courier Dover Publications, 2017).